Welding in the World (2024) 68:1443–1459
https://doi.org/10.1007/s40194-024-01684-x

RESEARCH PAPER

Suppression of spiking defects in deep penetration electron beam welded ETP copper

Konrad Kerber[1,2] · Lars Halbauer[3] · Horst Biermann[1,2] · Anja Buchwalder[4]

Received: 20 February 2023 / Accepted: 8 January 2024 / Published online: 26 January 2024

Abstract

The electron beam is an appropriate tool to weld pure copper due to its high absorptivity on the copper surface, a high power density and inert vacuum environment. However, deep penetration electron beam welding of pure copper often produces the spiking defect. In this work bead on plate electron beam welding was done on Cu-ETP. A critical welding speed was determined for the distinction between a conduction-determined (at lower welding speed) and a non-conduction-determined welding speed range (at higher welding speed). The influence of high preheating temperatures was shown. The welds were investigated by light optical microscopy, electron backscatter diffraction measurements, ultrasonic testing, in situ thermal imaging, electrical resistance measurements and tensile tests. It was shown that in the conduction-determined welding speed regime without preheating, full and partial penetration welds exhibited root porosity. This effect was related to the overheating of the weld pool in combination with the phenomena causing spiking. Low defect root formation was achieved by using welding speeds greater than the critical value or by applying high preheating temperatures. The joints reached up to 98% of the international annealed copper standard in terms of specific electrical conductivity. Rupture took place within the joints during tensile tests. The joints exhibited up to 77% of the ultimate tensile strength of the base metal. Welds carried out with preheating exceeded the base metal regarding the fracture strain.

Keywords Electron beam · Deep penetration welding · Pure copper · Spiking suppression

1 Introduction

The demand for copper shows a steady increase over the last few years. It is predicted to rise further [1, 2]. For component applications, it is essential to have a joining technology which preserves the desired material properties. This task can be achieved by welding. However, in the case of pure copper, welding is a challenging task due to the high thermal conductivity and expansion as well as high shrinkage [3]. This behavior results in high residual stresses and deformations in conventional welding processes [4–6]. The related problems can be avoided by the use of a high-energy source, e.g., the electron beam (EB). Its high power density [7] enables deep penetration welding, also called keyhole welding. Due to the high power density of the incident beam the material of a welded plate can be vaporized locally. This vaporization creates a vapor capillary, also known as keyhole, which penetrates the plate. The keyhole is surrounded by molten metal which is held back by the vapor pressure, also called recoil pressure, of the vaporized material. Due to the relative motion between the plate and the beam new material is vapor-

✉ Konrad Kerber
konrad.kerber@iwt.tu-freiberg.de

Lars Halbauer
lars.halbauer@manatec.de

Horst Biermann
biermann@ww.tu-freiberg.de

Anja Buchwalder
anja.buchwalder@fhnw.ch

1 Institut für Werkstofftechnik, TU Bergakademie Freiberg, Gustav-Zeuner-Str. 5, Freiberg 09599, Germany

2 Zentrum für effiziente Hochtemperaturstoffwandlung, TU Bergakademie Freiberg, Winklerstraße 5, Freiberg 09599, Germany

3 Present address: manaTec GmbH, Königsbrücker Str. 124, Dresden 01099, Germany

4 Present address: Institute for Product and Production Engineering (IPEE), University of Applied Sciences and Arts Northwestern Switzerland (FHNW), Klosterzelgstrasse 2, Windisch CH-5210, Switzerland

ized at the front of the keyhole. At the rear end of the keyhole the surrounding melt flows in and solidifies, creating a narrow weld. This process allows welding of thick plates within a single pass without a filler metal. Hence, the productivity in electron beam welding (EBW) is high. Deformations and residual stresses are small as the melt pool is narrow. Due to the lack of a filler metal no impurities are added into the weld [8–10]. Additionally, the inert vacuum environment prevents the dissolution of gases in the melt pool and reduces the formation of plasma in the beam path. Also, the absorbed energy of the EB is nearly independent of the surface characteristics for a given acceleration voltage and material and is usually higher than 75%. Therefore, the electron beam is an appropriate tool to weld pure copper [11, 12].

However, keyhole welding produces a wide range of defects that reduce the mechanical properties of the joint considerably. Typical defects are pores, melt ejections, cold-shuts and spiking [13–18]. The latter describes periodic deviations of the penetration depth which usually result in the other aforementioned defects [19, 20]. During full and partial penetration EBW of copper spiking was frequently observed. Therefore, it is considered to be critical for the quality of copper welds [21–24].

Over the last few decades spiking has been investigated intensively. The majority of studies suggested that it is caused by instabilities of the keyhole. Some authors concluded that spiking is inherent to welding with a keyhole due to the increase of closing forces with increasing penetration depth. Hence, the proposed method in order to reduce spiking was to minimize penetration depth [25–28]. Other studies suggested that spiking is caused by a periodic melt flow in the keyhole. This could be avoided by the addition of volatile alloying elements in the base metal, which increased the recoil pressure [13, 29]. However, there seems to be no generally positive effect of an addition of a volatile alloying element as the effect diminished in dependency of welded material and insertion position [30]. Also, Wei et al. [31] reported a greater spiking amplitude in welds of Al 5083 compared to welds of Al 6061 for different welding speeds and focal positions. In other models, the deviation of the penetration depth was due to the collapse of the vapor capillary. This collapse is brought about by knobs and cavities in the surrounding melt pool, which are caused by the dynamic melt pool flow. The protrusions interact with the beam and therefore reduce the recoil pressure in parts of the keyhole. This, in turn, disturbs the dynamic equilibrium at the gas/liquid-phase boundary and results in the aforementioned collapse. Afterwards, a new keyhole is formed and the process repeats, resulting in an oscillating penetration depth [30, 32–36]. In numerical investigations, these oscillations were simulated [37, 38]. It was shown that the collapsing part of the vapor capillary can remain in the weld seam as gas cavity. This effect regularly occurred, when the thermal conductivity of the base metal was high [20, 39–42].

Fetzer et al. [43] showed that spiking also occurred in the case of a stable keyhole. Only the occurrence of porosity was a result of the keyhole instability. In their model, spiking was caused by the alternation of the irradiation on the front of the keyhole. It was shown that the frequency of spiking linearly scales with the welding speed. Other studies showed a similar tendency [31, 44].

Linear and circular beam oscillations showed some success in reducing spiking for various metals [21, 45], which was mainly attributed to a more uniform melt flow [46]. Heider et al. [14, 47, 48] and Cho et al. [49] successfully used a sinusoidal power modulation to stabilize the vapor capillary. Moreover, spiking was successfully suppressed by increasing the welding speed [10, 50].

The current work was focused on the suppression of defects due to spiking in full and partial penetration EBW of ETP copper (electrolytic tough pitch copper, UNS C11000). The welds were characterized by macroscopic investigations, microstructure analysis using light optical and scanning electron microscopy (SEM) as well as measurement of the electrical resistance and mechanical properties.

2 Experimental details

2.1 Base metal

For all experiments, Cu-ETP (Hans-Erich Gemmel & Co. GmbH, Germany) was used as base metal (BM). The thickness d of the sheets was 4 mm and 10 mm. The chemical compositions (see Table 1) were determined using gas fusion analysis (Bruker G8 Galileo, O) and optical emission spectroscopy (ARL4460 Metal Analyzer, other elements).

Samples were cut in a uniform geometry of $80 \times 50\,mm^2$. The plates for tensile specimens had dimensions of $125 \times 50\,mm^2$. The specimens were brushed with an abrasive fleece and cleaned with acetone. Specimens for experiments with preheating were blasted with alumina powder with 120–150µm particle size. This process ensured a homogeneously rough surface for pyrometric temperature measurements.

Table 1 Chemical composition of the base metal with a thickness of 4 and 10 mm, mass fraction in ppm

d	Cu	Ag	Bi	O	Pb	∑ rem
4 mm	bal	7	→ 0	193	→ 0	192
10 mm	bal	12	1	9	1	74

2.2 Welding parameters and setup

The welding experiments were carried out with two electron beam facilities. Specimens with 10 mm thickness were welded in a pro-beam K26-80/15 at a constant acceleration voltage (U_{acc}) of 80 kV. Specimens with 4 mm thickness were welded in a pro-beam K40-150/30 at a constant acceleration voltage of 150 kV. In both vacuum chambers the pressure was 2×10^{-3} mbar. The weld length was 50 mm. Results for 10 mm thickness are marked separately. For welding speeds (v) > 80 mm s^{-1}, the welds were made using beam movement. Otherwise, the CNC-controlled axes inside the chambers were used to move the specimens. The welds were made at sharp focus. In order to improve the formation of the upper bead, selected specimens were subjected to a post welding smoothing process ($U_{acc} = 150$ kV, a beam current (I_b) of 10 mA, $v = 10$ mm s^{-1}, circular beam scanning with a diameter of 3 mm and a frequency of 3000 Hz).

For preheating, a heating field of 20×50 mm^2 with 100×250 equidistant interaction points was placed symmetrically around the zone that was welded afterwards. Each point had an interaction time of 110 ns. The temperature at the surface of the plate was measured with a two-color pyrometer, which was calibrated using a thermocouple. The pyrometer had a built-in PID-controller to control the beam current based on temperature using the control software SensorControl. The maximum beam current for preheating was set to 55 mA. A thermographic camera was set up above the specimens to measure the surface temperature distributions on the plates. The surface temperature within the pyrometer-spot was set to 900 C and was held for 20 s. Welding was done immediately afterwards. For details on the configuration of the pyrometer and thermographic camera see [51].

The beam current to fully penetrate the plates was determined for different welding speeds for specimens at room temperature (without preheating) and with preheating. As the spiking phenomenon caused individual craters to form, intersected by unaffected surfaces at the bottom of the plate, a weld was considered fully penetrated when the craters resulting from the spiking phenomenon were no longer intersected by unaffected surfaces, i. e. when the craters touched or were connected by solidified melt. A weld was also counted as fully penetrated, when a continuous root was formed. Also, a full factorial design for $v = 10,\ 20,\ 30$ and 40 mm s^{-1} and the line energies (calculated according to Eq. 1) $E = 120, 160, 200$ and 240 J mm^{-1} was carried out for $d = 10$ mm. The line energy refers to the energy input per weld length and is commonly used for EBW processes [10, 52–55].

$$E = \frac{I_b U_{acc}}{v} \tag{1}$$

2.3 Characterization methods

2.3.1 Macroscopic and microscopic analysis

The upper bead and the root were investigated using a stereo microscope. After welding, cross sections of the welds were prepared. For the determination of the weld geometries, three cross sections were analyzed. Longitudinal sections were cut in the center of the weld, perpendicular to the specimens' surface. The specimens were ground, polished and etched with a solution of 65 ml ethanol, 25 ml HCl (37%) and 4 ml H_2O_2. The specimens were etched for up to 15 s and cleaned with ethanol afterwards. For SEM investigations, the specimens were vibration polished (SiO-suspension with a particle size of 0.02 µm) for 24 h.

The etched specimens were examined by light optical microscopy (Olympus GX51). The SEM investigations were carried out with a MIRA 3 XMU TESCAN with an acceleration voltage of 20 kV, a working distance of 20 mm and a tilting of 70. The electron backscatter diffraction (EBSD) analysis was performed with the software OIM ANALYSIS 6.0. The white marked areas in Fig. 1 were scanned with a point distance of 5 µm. The minimal misorientation for the distinction between grains was set to 12.

The results for all depths (Fig. 1a) were combined into one grain area distribution for different welding speeds. The resulting distributions were compared using the Dunn test with Hochberg correction.

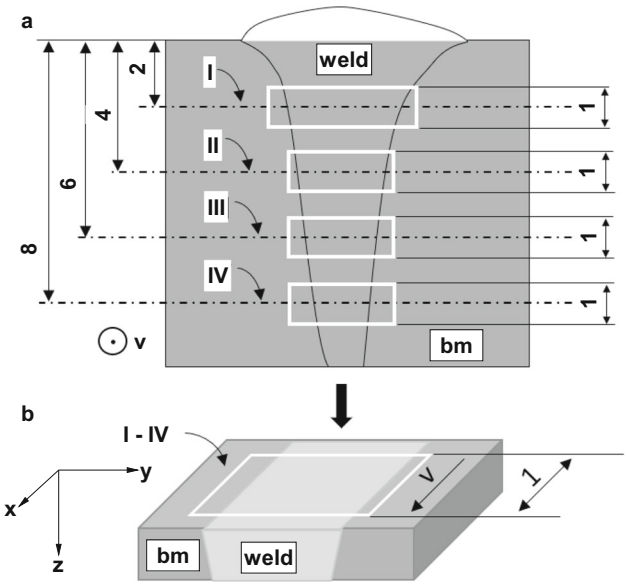

Fig. 1 Positions of the EBSD-scans (white marked sections with numbers I-IV) for **a** cross sections and **b** longitudinal sections, displayed values in millimeters

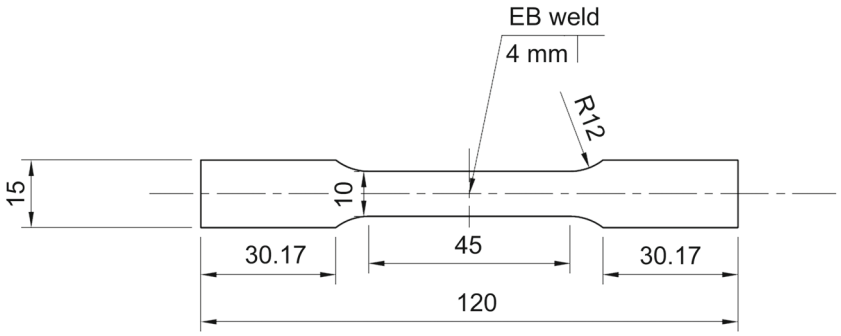

Fig. 2 Geometry of the tensile specimens, rectangular cross section ($10 \times 4\,mm^2$), displayed values in millimeters

2.3.2 Ultrasonic testing

For ultrasonic testing, longitudinal sections with a length > 10 mm were cut perpendicular to the plates' surface and parallel to the welding direction, and ground. The width of the sections was 8 mm, with the weld in the center. For further details regarding ultrasonic testing configuration, please refer to the experimental section of [56]. In the full factorial design concerning variables v and E in Sect. 2.2, the number of spikes was counted and normalized to the scanned weld length.

2.3.3 Tensile tests

Tensile specimens with a rectangular cross section ($10 \times 4\,mm^2$) were machined according to Fig. 2. The gauge length was 45 mm. The elongation was measured with an extensometer. Tests were done with an electromechanical testing device (inspekt desk 50, Hegewald und Peschke, Germany). The strain rates were chosen to be $7 \times 10^{-5}\,s^{-1}$ up to a plastic strain of 0.2% and $2 \times 10^{-3}\,s^{-1}$ afterwards, according to DIN EN ISO 6892-1.

The fracture strain was calculated based on the gauge length after the test.

2.3.4 Resistance measurements

The electrical resistance was measured using the four-point potentiostatic method (PROMET R300, Kocos) at a current of 100 A on specimens with the dimensions $80 \times 30 \times 4\,mm^3$. The measurement length was 8.8 mm. As the specific resistance of the weld was of interest, a connection in series of the weld and the base metal was assumed. Using Ohm's law and a weld width of 1.6 mm, the specific resistance of the weld was determined [24]. In addition, the Eddy current method was used in the middle of the weld seam (SIGMATEST 2.067, Foerster). The radius of the measurement area was 16 mm.

3 Results and discussion

3.1 Macroscopic phenomena

3.1.1 Definition of speed ranges

The beam currents to fully penetrate the plates were determined for different welding speeds. Figure 3 shows the required beam currents to fully penetrate the plate for different welding speeds, when the specimen was at room temperature prior to welding (without preheating) and after preheating according to Sect. 2.2.

Both curves agree well with a linear relationship. As to be expected, the required beam current is lower for the preheated specimens. The line energy E, calculated according to Eq. 1 from the beam currents and the respective welding speed, yields the curves displayed in Fig. 4.

In Fig. 4a, E is plotted against the welding speed. For plates at room temperature, the required line energy to pen-

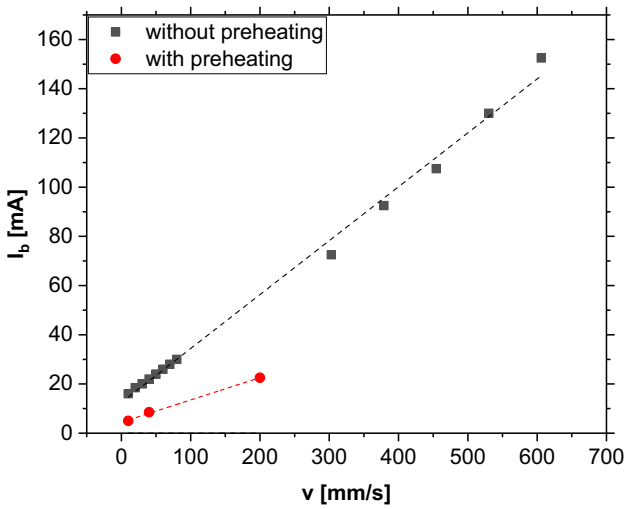

Fig. 3 Required beam current I_b to fully penetrate a 4-mm-thick plate for different welding speeds v with and without preheating (U_{acc} = 150 kV)

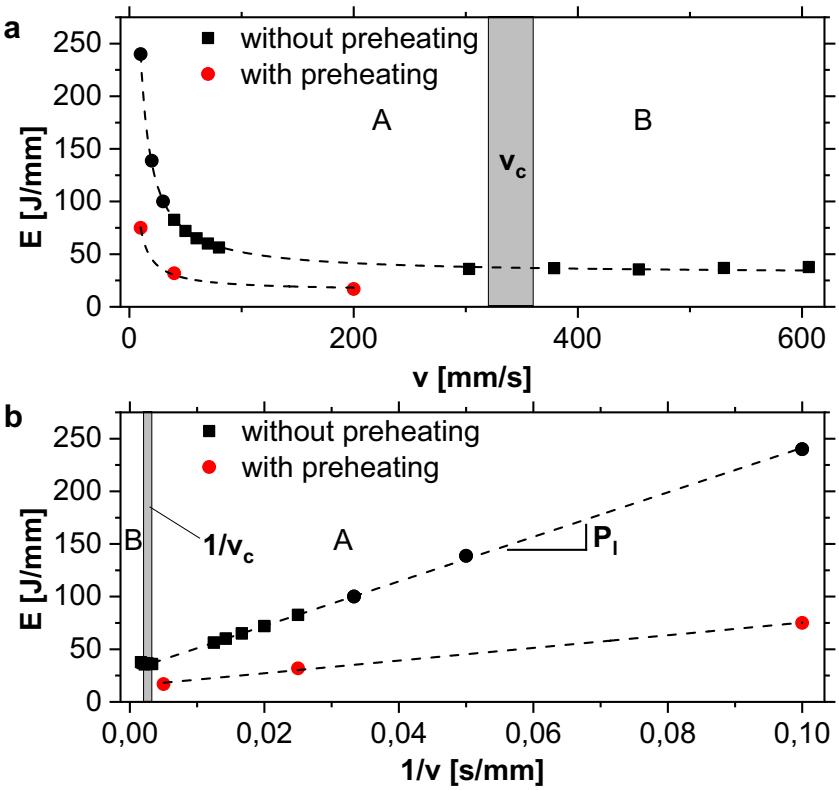

Fig. 4 E to penetrate a 4-mm-thick plate for **a** different welding speeds (v), **b** for reciprocal welding speeds ($1/v$)

etrate the plate shows a hyperbolic curve. The line energy remains nearly constant for high welding speeds. Plotting the required line energy against the reciprocal welding speed yields Fig. 4b. Clearly, the required energy to penetrate the plate depended on the time spent per weld length. The curves can be divided into two distinct areas (see areas A and B in Fig. 4). In area A, at higher time unit per weld length, the line energy closely follows a linear relationship on the reciprocal welding speed for both, the specimens with and without preheating. The slopes of the regression lines, $2115\,\mathrm{J\,s^{-1}}$ and $602\,\mathrm{J\,s^{-1}}$ respectively, can be interpreted as an integral power loss P_l of the keyhole within the welding process. P_l was far lower for welds done with preheating, because smaller amount of heat conducted into the base metal. As welding was done in vacuum, only radiation occurred at the surface of the plate. The resulting power losses were negligible. Therefore, the radial power losses of the keyhole and its surrounding melt pool (assuming the axial direction is along the penetration depth) determined P_l. These losses mainly depended on the surface area to the base metal for a set keyhole and melt pool geometry [57, 58].

When the welding speed was increased above a critical value v_c, i. e. the time spent per unit weld length was decreased below a critical value $1/v_c$, P_l becomes zero (area B in Fig. 4b). The energy to penetrate the plate then was independent of the time spent per weld length. The critical speed was determined by inserting the value of the line energy from area B (Fig. 4) in the linear regression equation from area A. This yielded a critical welding speed of $v_c \approx 320\text{–}350\,\mathrm{mm\,s^{-2}}$.

This transition can be explained by the change of radial energy loss. As the welding speed increased, the time for radial heat flow diminished (see Fig. 4b). Furthermore, the heat flux due to the released heat of fusion increased, which decreased the temperature gradient at the rear of the melt pool [59].

As long as the line energy to penetrate the plate depended on the time per weld length ($v < v_c$), the radial heat conduction determined the required beam power for full penetration. Hence, this speed regime (area A in Fig. 4) is called the conduction-determined weld speed regime (CD speed regime). If $v > v_c$ (area B in Fig. 4) the interrelationships were vice versa, hence the speed regime is called non-conduction-determined weld speed regime (NCD speed regime).

3.1.2 Weld geometry

For $v < v_c$, in the CD speed regime without preheating, the integral power loss was shown to be constant. If the constancy of P_l is mainly attributed to a change in radially conducted heat, there should be no significant changes in the dimensions of the weld pool at a given plate temperature with a varying

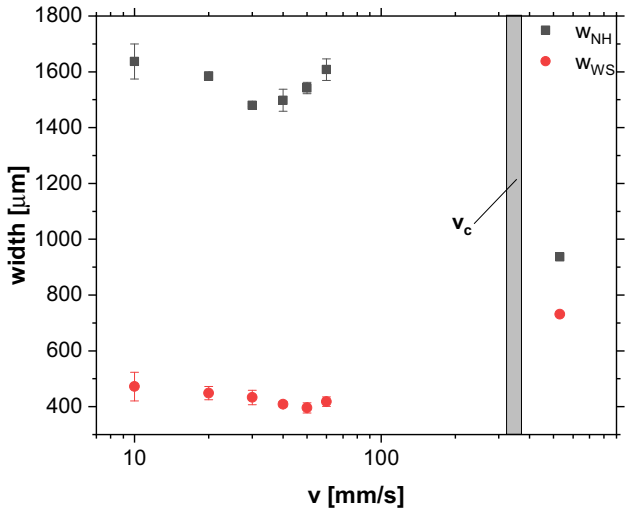

Fig. 5 Geometrical parameters of the fully penetrated welds without preheating for different welding speeds (v) with MAD

weld speed. In Fig. 5, the width of the nail head (w_{NH}, width of the weld at the top of the plate) and the width at half penetration depth (w_{WS}) are plotted with the mean absolute deviation around the mean (MAD) as error bars for different welding speeds.

Statistical analysis in Table 2 shows that w_{NH} exhibited no significant differences for lower and higher welding speeds.

This indicates that the weld pool formation, which was mainly determined by heat conduction processes at the top of the plate, was nearly identical for different welding speeds in the CD speed regime. w_{WS} shows significant differences between lower and higher welding speeds (Table 2). However, in contrast to w_{NH}, w_{WS} is far more sensitive to fluctuations of the keyhole, the absolute beam power and differences in input power as the closing forces are higher [60, 61]. It has also to be mentioned that the determination of a fully penetrated weld was somewhat subjective. This can also result in deviations, especially for sensitive parameters. Hence, these differences are not seen as a measure for the radial power loss due to heat conduction.

If the heat flux due to the released heat of fusion is far smaller than the amount of energy which is transported radially and the amount of heat conduction welding is nearly identical, the length of the trailing weld pool does not depend on v in the CD speed regime. As the thermal conductivity of the base metal is very high (394 $\mathrm{W\,m^{-1}\,K^{-1}}$ [62]), a small heat flow due to the released heat of fusion, by comparison, is reasonable to be assumed (for more details see [59]) as long as $v << v_c$. It has to be mentioned that w_{NH} also depends on the convective heat transport. For high alloyed steel, Peclet numbers between 1 and 15 were reported [59, 60]. However, this number should be lower for pure copper, due to the far higher thermal conductivity (for details regarding the Peclet number during keyhole welding see [63]). Nevertheless, an increase of convective heat transport with increasing v might contribute to a constant P_l.

In the case of $v > v_c$, in the NCD speed regime without preheating, w_{NH} decreases and w_{WS} increases (Fig. 5). The former indicates that the radial heat conduction was diminished. The latter might be a result of an increased absolute power density.

3.1.3 Upper bead and root formation

The formation of the upper bead and root of the welds in the respective welding speed regime was investigated by stereo microscopy. The spikes were analyzed by light optical microscopy and ultrasonic testing. Figure 6 shows a representative upper bead and a representative longitudinal section with spiking defects of a partially penetrated weld (Fig. 6a and c). In Fig. 6b, the mean number of spikes per millimeter weld, along with the corresponding mean spiking frequency for different welding speeds in the CD speed regime without preheating is displayed. Figure 7 shows the upper bead and the root for a fully penetrated weld at $v = 40\,\mathrm{mm\,s^{-1}}$ without preheating. In the previous section it was shown that the effect of welding speed on w_{NH} was small in the CD speed regime. When welding in the CD speed regime ($v < v_c$) without preheating the scaling of the upper bead had a semicircular shape for all tested welding speeds (Figs. 6a and 7a). Hence, the effect of the welding speed on the shape of the rear end of the weld pool at the surface was small in the CD speed regime.

Table 2 Results of the statistical analysis of the weld geometry for $v < v_c$

groups	test	statistic	p-value
$w_{NH}(v = 10, 20, 30\,\mathrm{mm\,s^{-1}})$	Shapiro-Wilk test	0.9618	0.8273
vs	Levene test	0.5739	0.4605
$w_{NH}(v = 40, 50, 60\,\mathrm{mm\,s^{-1}})$	t-test	0.8262	0.4217
$w_{WS}(v = 10, 20, 30\,\mathrm{mm\,s^{-1}})$	Shapiro-Wilk test	0.9407	0.6182
vs	Levene test	3.6859	0.0741
$w_{WS}(v = 40, 50, 60\,\mathrm{mm\,s^{-1}})$	t-test	2.6815	0.0171*

$\alpha = 0.05$, * marks significant results

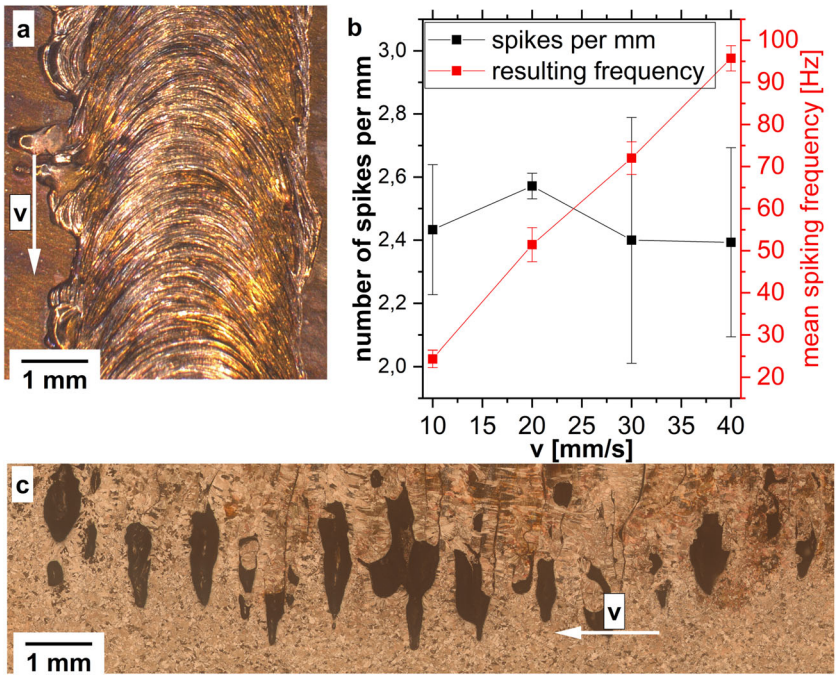

Fig. 6 Representative **a** upper bead at $v = 30\,\mathrm{mm\,s^{-1}}$ for a partially penetrated weld in the CD speed regime, **b** mean number of spikes per millimeter of weld and the mean resulting spiking frequency in dependency of the welding speed with MAD, **c** representative spiking for a partial penetration weld at $v = 30\,\mathrm{mm\,s^{-1}}$ without preheating

The roots for partially and fully penetrated welds without preheating in the CD speed regime exhibited defects (Figs. 6c and 7b). In the former case, this can be seen by significant root porosity caused by spiking (Fig 6c). The number of spikes per unit weld length was nearly constant for all tested welding speeds (Fig. 6b). Hence, the mean spiking frequency scaled linear with the welding speed (Fig. 6b). This means that the time scale for the spiking phenomena to occur was inversely proportional to the welding speed, which is in good agreement with results reported in literature [31, 43]. For fully penetrated welds, there was a visible formation of a root (see arrows in Fig. 7b). However, it was disrupted by periodical, circular melt ejections. Comparing the porosity caused by spiking in Fig. 6c to the craters in Fig. 7b yields the following conclusion: The disruption of the root for fully penetrated welds was due to an increase of recoil pressure, which blows out the melt at the bottom side of the plate. The literature agrees very well on the fact that spiking was caused by an increase in recoil pressure [29, 30, 32–34, 40, 43]. Therefore, it is reasonable to assume that the disruption of the root for full penetration welds and the observed spiking for partial penetration welds are caused by the same phenomena. Usually root defects can be avoided by fully penetrating the plate [10, 37, 64, 65]. However, this was not possible for pure copper. In literature, the main reasons reported for this effect are a small solidification temperature range, a low surface tension and viscosity combined with a high thermal conductivity [23, 24].

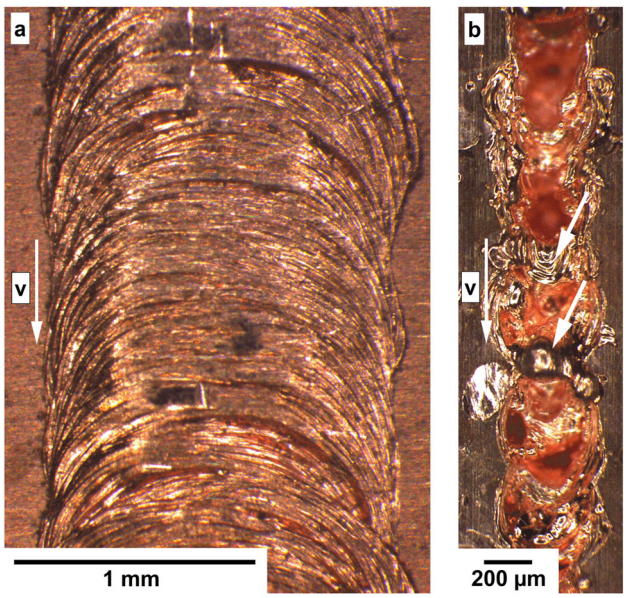

Fig. 7 **a** Upper bead and **b** root at $v = 40\,\mathrm{mm\,s^{-1}}$ for a fully penetrated weld in the CD speed regime without preheating

Figure 8 shows both the upper bead and the root of a weld without preheating at a very high welding speed ($v = 530\,\mathrm{mm\,s^{-1}}$) in the NCD speed regime.

In contrast to the results in the CD speed regime without preheating, there was a visible root formation for welds made in the NCD speed regime (compare Figs. 7b and 8b). However, the root formation was accompanied by melt ejections at the upper bead and humping at the root (Fig. 8a and b). It can be assumed that the very high power density required to achieve the penetration leads to melt eruptions, when interacting with the closing melt as shown earlier [66, 69–73]. Humping was frequently reported in literature and

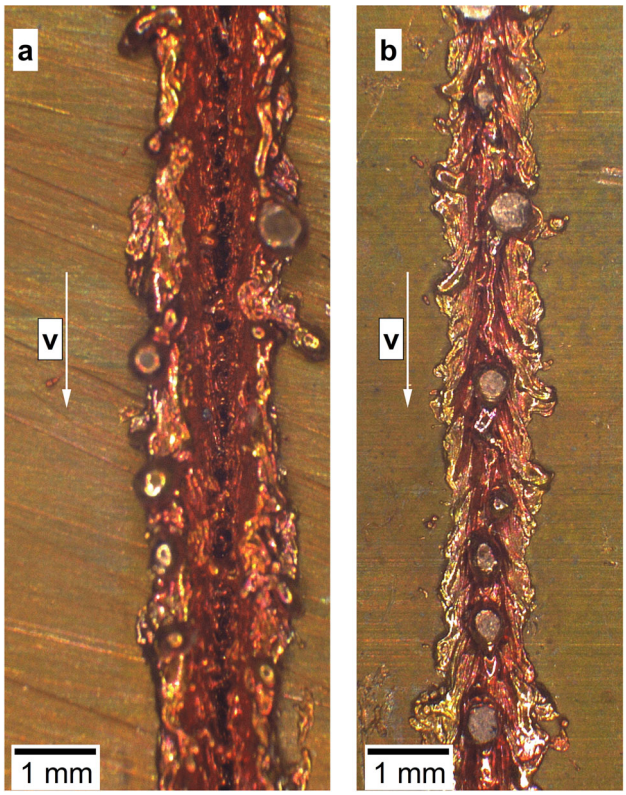

Fig. 8 **a** Upper bead and **b** root of a representative weld with $v = 530\,\mathrm{mm\,s^{-1}}$ without preheating

extensive work has been done to understand the physical phenomena behind it [31, 67, 68]. It was shown that root humps are formed, when the weld pool spreads at the root [65]. This may be also the reason for the root formation in the NCD speed regime. The topography of the root in Fig. 8b shows that the melt was ejected from the bottom of the plate. Also, typical splatters were observed at the bottom of the plate after welding. However, in contrast to welds made in CD speed regime, for $v > v_c$ the weld pool was elongated due to the high heat flux caused by the released heat of fusion [59]. Therefore, molten metal could flow into the cavities of the previously shown spikes (see Fig. 6c). This also contributed to the volume deficit at the upper bead [65].

Figure 9 shows the upper bead and the root of welds at $v = 40\,\mathrm{mm\,s^{-1}}$ in the CD speed regime with preheating at different beam currents ($I_b = 8.5\,\mathrm{mA}$ and $10.0\,\mathrm{mA}$).

Both welds show an upper bead without humping (see Fig. 9a and c) as well as a root free of craters caused by spiking (see Fig. 9b and d). The proper root formation for preheated welds can be explained by the changes in radial power loss (shown in Sect. 3.1.1). As mentioned in the literature, pure copper exhibits unfavorable thermophysical properties for EBW, i.e., high thermal conductivity, low viscosity and low surface tension [23, 24]. This means that due to high radial power loss without preheating (Sect. 3.1.1) a very high beam power is required to achieve a desired penetration depth. This results in an overheated weld pool and high evaporation rates, i.e., high recoil pressures. In literature, the former is reported to yield sagging at the root of an Al alloy [65]. In this context, the shown melt ejections are just a case of sagging due to an overheated weld pool, amplified by increases in recoil pressure due to the phenomena causing spiking. The relatively high density of copper, which results in a high hydrostatic pressure, fits in this assumption as well. By decreasing the radial power loss via preheating, the required beam power was significantly reduced (shown in Fig. 3). A lower required beam power reduces the aforementioned over-

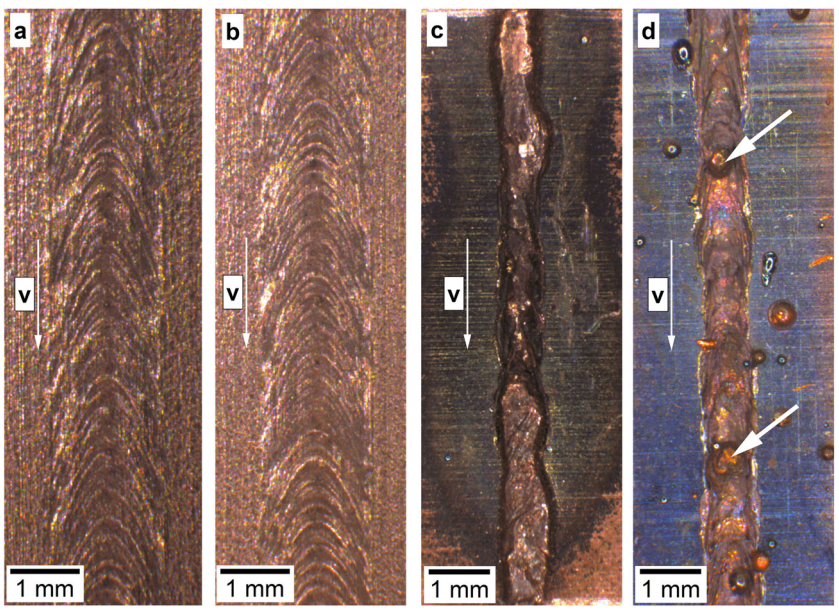

Fig. 9 Upper bead and root of welds at $v = 40\,\mathrm{mm\,s^{-1}}$ with preheating at **a**, **b** $I_b = 8.5\,\mathrm{mA}$ and **c**, **d** $I_b = 10.0\,\mathrm{mA}$

heating of the weld pool and the high evaporation rates. The former increases the viscosity and the surface tension of the melt. The latter reduces the recoil pressure. Thus, the melt is not blown out at the bottom of the plate and a root was formed. A further increase of the beam power (increasing I_b from 8.5 mA to 10.0 mA) results in melt ejections and splatters (compare Fig. 8b and d, arrows mark melt ejections).

To further investigate the influence of welding speed and preheating on the upper bead and root formation, thermographic imaging was done in situ on welding processes with and without preheating using a thermographic camera. Figure 10 shows the weld pools and their respective temperature profiles at the top of the plate of welds with and without preheating in the CD speed regime ($v = 40\,\mathrm{mm\,s^{-1}}$).

Both welds showed instabilities of the keyhole during the welding process (opening and closing of the keyhole in Fig. 10a and b). As the weld without preheating exhibited defects associated with spiking, while the weld with preheating did not, a stabilization of the keyhole seems not paramount for their prevention. This agrees well with findings of Fetzer et al. [43]. The dimensions of the weld pool for preheating were slightly larger in vertical direction (Fig. 10c). However, the profiles were rather symmetrical. Parallel to the welding direction, the temperature profiles without preheating exhibited nearly identical dimensions over the welding process (compare Fig. 10c and d). This observation proves the nearly circular shape of the weld pool and the earlier statement from Sect. 3.1.1, regarding the insignificant heat flux due to released heat of fusion in the CD speed regime. The temperature profiles changed significantly for the welds done with preheating (Fig. 10d). Firstly, the weld pool was slightly elongated, which can also be seen by comparing Fig. 10a and b. Secondly, the temperature profiles along the x-axis showed a plateau close to the liquid-phase boundary, which increased in size over the welding time (arrows in Fig. 10d) due to the accumulation of latent heat closely behind the weld pool [59]. Hence, the elongation of the weld pool could also contribute to the proper root formation on preheated welds (see Fig. 9b and d). This is sensible as a larger volume of trailing melt with lower temperature, i.e., higher viscosity and surface tension, is available for root formation.

So far the suppression of spiking defects during EBW was only shown for fully penetrated welds. For this case the spreading of the weld pool at the lower end of the plate could contribute to the suppression of defects [10, 37, 64, 65]. Hence, partial penetration welds with and without preheating were investigated using ultrasonic testing in both speed regimes. Figure 11 shows the defect indications of ultrasonic tests done at partial penetration welds. Figure 11a and b show welds at $v = 40\,\mathrm{mm\,s^{-1}}$ in the CD speed regime without preheating and with preheating respectively. Figure 11c shows a weld at $v = 200\,\mathrm{mm\,s^{-1}}$ with preheating. Regarding the latter, a thermographic image with the respective temperature profiles of the weld pool is shown in Fig. 12.

The weld without preheating exhibited the already shown root porosity due to spiking. For welds with preheating, this porosity was greatly diminished (Fig. 11b, arrows). This is understandable, as the power density was far lower compared to welds without preheating (cf. Sect. 3.1.1, for details see [25–27, 31, 44]). For welds generated with preheating at $v = 200\,\mathrm{mm\,s^{-1}}$, spiking defects were suppressed (Fig. 11c) as a result of a sufficiently elongated weld pool, cf. Fig. 12.

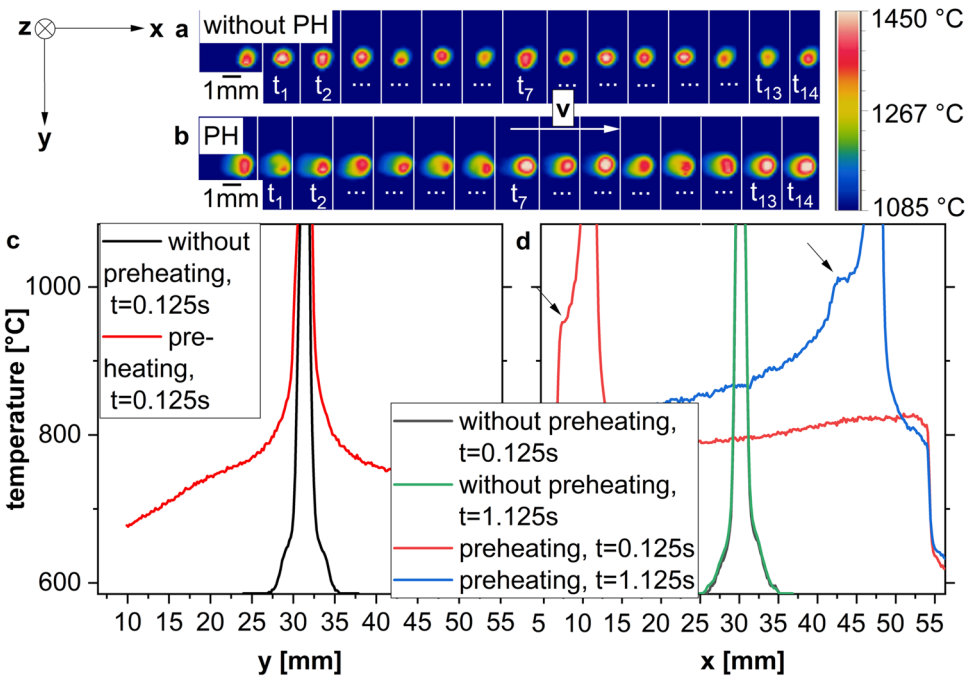

Fig. 10 Thermographic measurements of the melt pools for welds **a** without preheating and **b** with preheating and the associated temperature profiles with respect to $\vec{v}$ at different points in time of the welding process (0.1 *s* and 1 *s*) along the **c** y-axis and **d** x-axis at $v = 40\,\mathrm{mm\,s^{-1}}$, arrows mark plateaus due to latent heat accumulation. Each shown melt pool resembles a time step ($t_0 - t_{14}$) of 12.5 ms

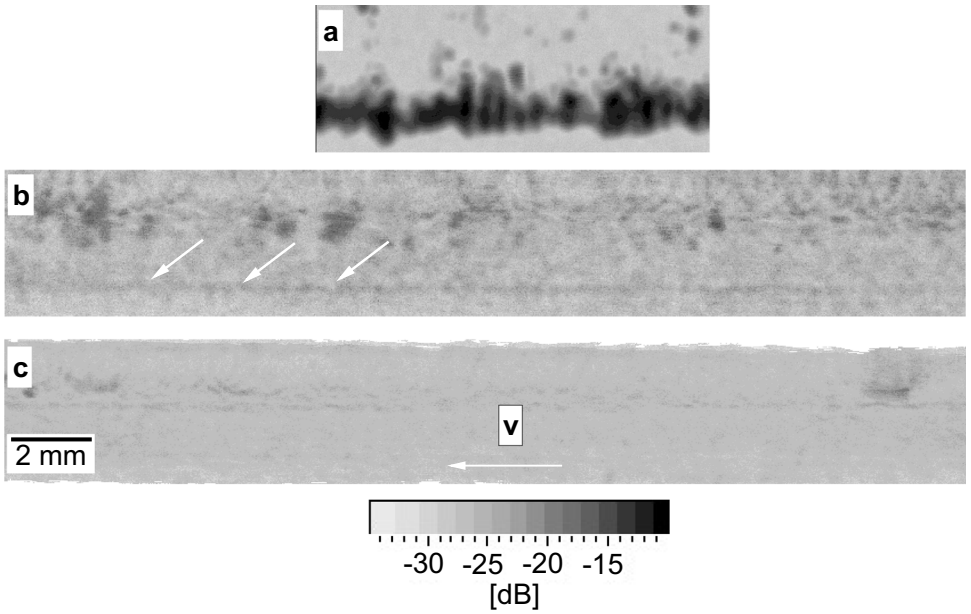

Fig. 11 Defect indications from ultrasonic test of the welds generated with $v = 40\,\mathrm{mm\,s^{-1}}$ **a** without preheating and **b** with preheating. **c** Defect echo for a weld with $v = 200\,\mathrm{mm\,s^{-1}}$ and preheating

The length was far larger than for lower welding speeds (compare Figs. 10 and 12). For welds with preheating, the suppression of spiking defects was obtained without melt ejections or serious humping at the upper bead (Fig. 11c), because the required welding speed to achieve the elongation of the melt pool was lower compared to welds without preheating due to the reduced radial power loss. Also the required beam power and therefore the power density were lower. The latter could have been detrimental to avoid the aforementioned melt ejections.

Based on the findings presented, it can be concluded that the suppression of spiking defects during EBW is achievable by creating a sufficiently long trailing weld pool while also minimizing the necessary beam power to achieve the desired penetration depth. The former enables the filling of pores or craters due to the keyhole oscillation. The latter reduces the recoil pressure to avoid melt ejections at the upper bead and the root. Both criteria aim at a trailing weld pool with minimal overheating, i.e., maximized viscosity and surface tension. In other studies, these criteria were achieved for a 16Cr-6Mn-9Ni steel by simply increasing the welding speed into the NCD speed regime [10]. In the case of pure copper, the addition of Sn was sufficient [24]. In this study, without a filler, a combination of preheating and a sufficiently high welding speed was necessary to achieve these conditions and suppress the spiking defects. The necessary welding speed was higher for partially penetrated welds.

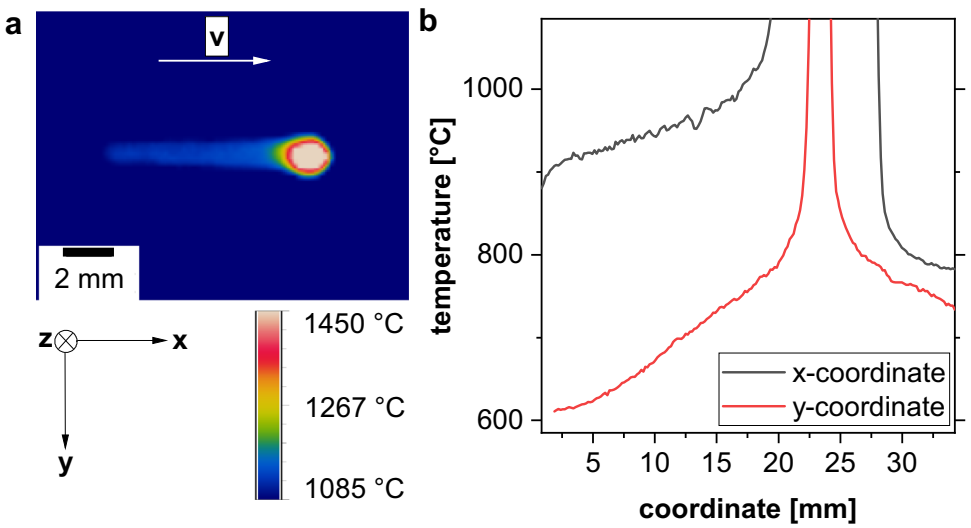

Fig. 12 **a** Melt pool for a weld with preheating at a welding speed of $200\,\mathrm{mm\,s^{-1}}$ and **b** the associated temperature profiles along the x-axis and y-axis

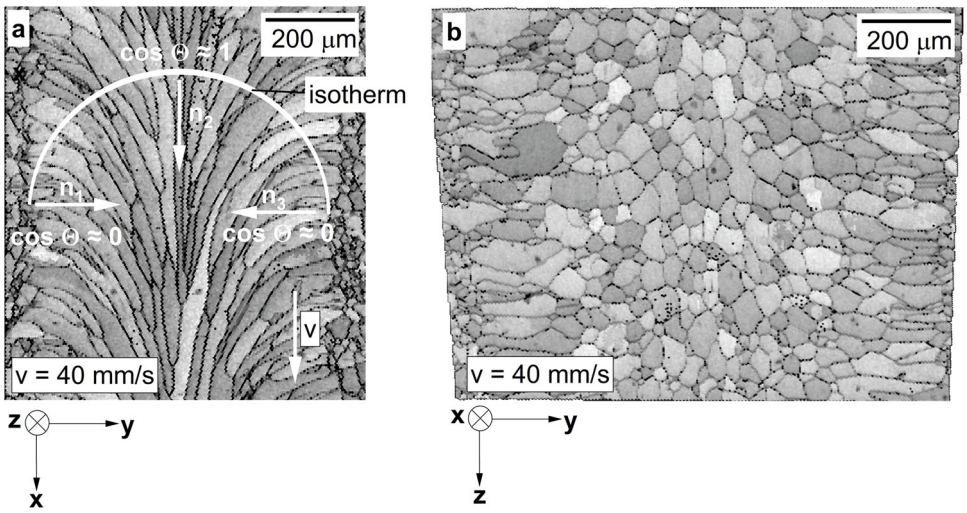

Fig. 13 Representative EBSD image quality maps of the microstructure at **a** the longitudinal section with schematic perpendiculars n_1-n_3 to the isotherm of the rear end of the weld pool and **b** the cross section

3.2 Characterization of the microstructure

The microstructure of the welds generated in both speed regimes without preheating was investigated by optical microscopy and SEM. Figure 13 shows representative microstructures of welds in the CD speed regime for different viewing directions relative to the welding direction.

Figure 13a shows that the grains nucleated epitaxially form the non-melted grains (for details see [69]). It is well established that for low welding speeds the solidification speed (v_s) can be written as a function of v and the angle Θ (angle between the perpendicular of the isotherm of the rear end of the weld pool and the welding direction, see n_1 - n_3 in Fig. 13a) (Eq. 2 [69]).

$$v_s = v cos\Theta \tag{2}$$

In the context of this work, low speeds are in the CD speed regime. The orientation of the grains depicted in Fig. 13a agreed well with the relation given by Eq. 2. As the isotherms at the rear end of the weld pool were semi-circular at temperatures near the melting point of copper in the CD speed regime (cf. Fig. 10a), the solidification speed in the directions n_1 and n_3 in Fig. 13a was comparatively small as Θ approached $\pi/2$ and $-\pi/2$ respectively. As Θ decreases, v_s increases, reaching its maximum in direction n_2 in Fig. 13a.

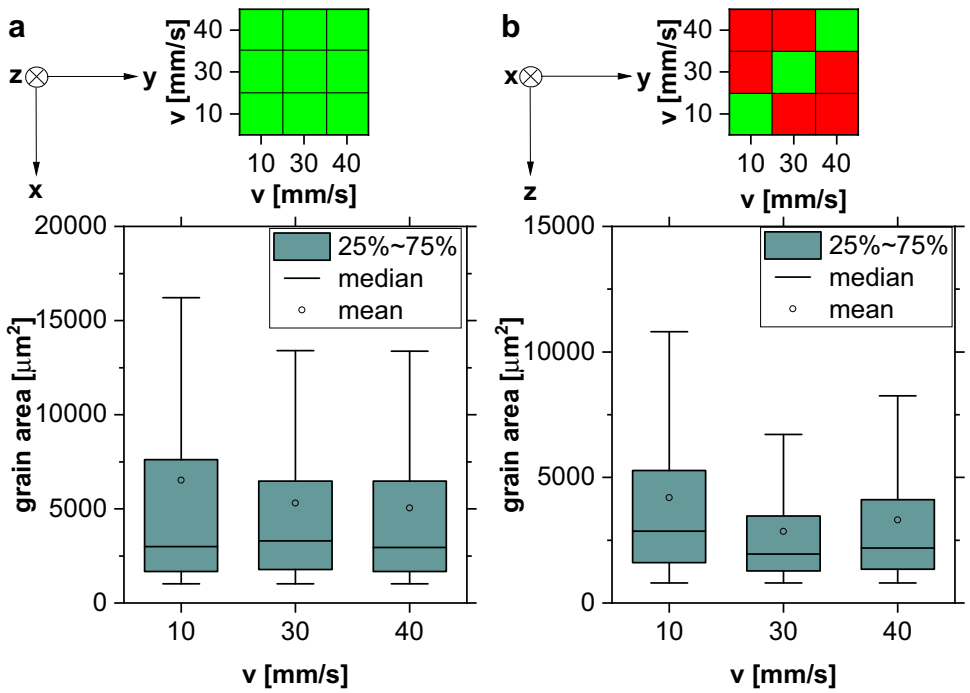

Fig. 14 Box plots of the grain area distributions for different welding speeds with test matrix for pairwise comparison by Dunn test at **a** the longitudinal section and **b** the cross section of the welds. Red — significant difference, green — no significant difference

Hence, the resulting growth direction resembles a curve when the beam passes. For details, refer to [69].

In Fig. 14a box plots of the grain area distributions along the longitudinal sections are plotted for different welding speeds in the CD speed regime.

A pairwise comparison by Dunn test showed that the grain area exhibited no significant differences for a changing welding speed, cf. Fig. 14a. As shown above, the melt solidified mainly epitaxially and Eq. 2 was valid. So, neither the nucleation mechanism nor the solidification morphology depended on v_s. Hence, a change in welding speed (for $v < v_c$) only increased the solidification speed according to Eq. 2. The grain area distribution depended on the geometry of the weld pool. As stated above, the melt pool was of circular shape for welds generated in the CD speed regime (see Sect. 3.1.3). The weld pool exhibited significant differences in width (see Sect. 3.1.2) along the penetration depth. However, as the main growth direction was parallel to the welding direction (cf. Fig. 13a and b), these differences were insignificant with regards to the grain area.

The grain area distributions at the cross sections perpendicular to the welding direction exhibited significant differences (Fig. 14b) due to the fact that the grain area was measured in the plane perpendicular to the main growth directions (cf. Fig. 13). Therefore, the changes in width, given in Sect. 3.1.2, became significant. This effect can be understood by looking at the isotherm in Fig. 13a. When the semi-circular isotherm is widened or narrowed, the number of grains that are then cut perpendicular to their longest direction of extension, which appear as nearly equiaxed grains in the cross section (see grains in the center of Fig. 13a), changes compared to the grains that are cut parallel to their longest direction of extension (see edges of the weld in Fig. 13a).

Figure 15 shows the optical micrograph of a cross section of a weld produced in the NCD speed regime without preheating ($v = 530\,\mathrm{mm\,s^{-1}}$).

In contrast to the CD speed regime (cf. Fig. 13b), the weld showed two solidification fronts, which grew together in the middle of the weld. This fact was due to the elongation of the weld pool, shown above in Sect. 3.1.3. This circumstance led to a solidification with a certain distance to the interaction point of the beam. Hence, the direction of the solidification was no longer dependent on the welding speed, i.e., Eq. 2 was no longer valid in the NCD speed regime. As heat was mainly dissipated into the base metal (see Sect. 3.1.1), the isotherms of the melt pool at temperatures near the melting point of copper became nearly parallel to the surrounding material (this effect can be seen in Fig. 12a). This type of solidification could be observed on the entire cross section of the weld (Fig. 15). Hence, the weld pool was elongated along the entire cross section of the weld.

Fig. 15 Light optical micrograph of an etched cross section of a weld generated with $v = 530\,\mathrm{mm\,s^{-1}}$

3.3 Electrical and mechanical properties

The electrical conductivity of the welds was calculated using the measured electrical resistance of the four-point potentiostatic method for selected welds or measured using the Eddy current method. Table 3 gives the specific electrical conductivity (σ) of the base metal of welds produced at $v = 40\,\mathrm{mm\,s^{-1}}$ with and without preheating and welds in the NCD speed regime $v = 530\,\mathrm{mm\,s^{-1}}$ including smoothed specimens (SM) without preheating, compared to reported data for different welding processes from the literature. The width of the area, over which the specific conductivity was averaged (w_m), is given for comparison (if available).

Table 3 Specific electrical conductivity (σ) for different welds compared to the literature

Process	Condition	w_m [mm]	σ [MS/m]	σ [%BM]	Ref
EBW	without preheating, $v = 40\,\mathrm{mm\,s^{-1}}$	1.6	55.2	96.3	-
EBW	without preheating, $v = 530\,\mathrm{mm\,s^{-1}}$	1.6	46.3	80.9	-
EBW	without preheating, $v = 530\,\mathrm{mm\,s^{-1}}$, SM	1.6	53.8	94.0	-
EBW	preheating, $v = 40\,\mathrm{mm\,s^{-1}}$	32.0	58.6*	101.8*	-
	BM		57.2 or 57.6*		
EBW	without preheating + Sn-Layer	2.0	40.7	67.0	[24]
	BM (Cu-DHP)		60.7		[24]
MIG	without preheating	-	18.0*/16.0*	31.0*/27.6*	[6]
LMIGHW	without preheating	-	39.0*/23.0*	67.2*/39.7*	[6]
	BM (T2 Copper)		58.0*		[6]
LBW	without preheating	8.0	-	97.5*	[70]
DPLBW	without preheating	8.0	-	97.5*	[70]
	BM (T2 Copper)		-		[70]
LBW	without preheating	8.0	59.3*/58.8*	101.2*/100.3*	[71]
	BM (T2 Copper)		58.6*		[71]
NVEBW	without preheating	10.0	-	94.7	[72]
	BM (ETP Copper)		-	94.7	[72]

Two values are shown when there was data for the upper bead/root side respectively, *measured with Eddy current method (w_m = diameter of the measurement area), SM for a smoothed specimen, MIG — Metal inert gas welding, LMIGHW — Laser MIG hybrid welding, LBW — Laser beam welding, DPLBW — Dual pass LBW, NVEBW — Non vacuum EBW

The specimen welded without preheating in the CD speed regime had a slight drop of the conductivity ($55.2\mathrm{MS\,m^{-1}}$) compared to the base metal ($57.2\mathrm{MS\,m^{-1}}$), which is due to the melt ejections at the root shown in Sect. 3.1.3. The eddy current measurements for the specimen with preheating in the CD speed regime showed an increased conductivity ($58.6\mathrm{MS\,m^{-1}}$) compared to the base metal. However, the changes in microstructure as well as the far larger w_m have to be taken into account, which could result in a compensation of counteracting effects. The specimens welded in the NCD speed regime ($v = 530\,\mathrm{mm\,s^{-1}}$) without preheating exhibited a greater drop due to the severe melt ejections ($46.3\mathrm{MS\,m^{-1}}$). However, the conductivity was increased to $53.8\mathrm{MS\,m^{-1}}$ by a subsequent smoothing (see Table 3, $530\,\mathrm{mm\,s^{1-}}$ SM). Overall, the specific electrical conductivity was higher compared to processes which used an additional filler (MIG, LMIGHW and EBW + Sn-Layer), as the copper remained pure. Compared to the welding processes without filler, there are only small differences (the differences in w_m have to be taken into account) and the conductivity of the BM was nearly preserved (cf. Table 3 EBW, LBW, DPLBW).

The ultimate tensile strength and the fracture strain of selected welds were measured using tensile tests. Table 4 gives the ultimate tensile strength (UTS) and the fracture strain for welds produced with $v = 40\,\mathrm{mm\,s^{-1}}$ in the CD speed regime with and without preheating compared to the base metal (specifications for Cu-ETP according to DIN EN 13599) and values from the literature reported for different welding processes.

Both welds exhibit a lower ultimate tensile strength (UTS) compared to the base metal (207 MPa, 216 MPa and 280 MPa for preheating, without preheating and BM respectively). The fracture strain was lower for the welds produced without preheating (3.9%), but higher for welds made with preheating (25%) compared to the base metal (14.1%). Fracture always took place within the weld. Nevertheless, the scatter of the mechanical properties of the welds was less than ±2%, which shows the good reproducibility of the welding process. For the welds made without preheating, the reason for the low ductility is clear, as the lower mechanical properties can be explained by the root defects. In the case of welds produced with preheating the reduction in strength can be attributed to defects as well as to softening caused by a lower dislocation density and coarse grains due to recrystallization and grain growth (preheating was done at 86% of the melting point). When comparing the welds done with preheating to the specifications, the welds exhibited slightly lower strength than the minimum value of R220 (207 MPa compared to 220 MPa). The fracture strain was between the values of the standards of R220 and R240 (cf. Table 4). Hence, there was a negative influence of the welding process on the mechanical properties. This is reasonable, as the keyhole was shown to be unstable (Sect. 3.1.3). As the base metals often varied in their reported mechanical properties, no direct comparisons

Table 4 Ultimate tensile strength and fracture strain (gauge length of 45 mm) for welds generated in the CD speed regime with preheating and without preheating compared to the base metal, values of standards (*according to DIN EN 13599) and values from the literature, MIG — Metal inert gas welding, LMIGHW — Laser MIG hybrid welding, LBW — Laser beam welding, DPLBW — Dual pass LBW, NVEBW — Non vacuum EBW, LCMTHW — Laser-cold metal transfer arc hybrid welding, FSW — Friction stir welding, CCGTAW — Constant current gas tungsten arc welding, PCGTAW — Pulsed current gas tungsten arc welding

Process	Condition	UTS [MPa]	fracture strain [%]	Ref
EBW	without preheating, $v = 40\,\mathrm{mm\,s^{-1}}$	215.6 ± 3.0	3.9 ± 0.2	-
EBW	preheating, $v = 40\,\mathrm{mm\,s^{-1}}$	206.9 ± 1.4	25.1 ± 0.6	-
Cu-ETP	BM	279.6 ± 0.3	14.1 ± 0.4	-
	R220*	220.0	≥ 42.0	[73]
	R240*	240.0	≥ 15.0	[73]
EBW	without preheating + Sn	204.9 ± 3.6	42.0	[24]
Cu-DHP	BM	220.0	42.0	[24]
MIG	without preheating	190.0	-	[6]
LMIGHW	without preheating	204.0	-	[6]
	BM (T2 Copper)	276.0	-	[6]
LBW	without preheating	200.8	3.9	[71]
	BM (T2 Copper)	248.8	25.0	[71]
LBW	without preheating	219.0	2.8	[70]
DPLBW	without preheating	207.0	2.9	[70]
	BM (T2 Copper)	266.0	26.6	[70]
LBW	without preheating	155.0 ± 10.0	4.5 ± 2.0	[74]
LCMTHW	without preheating	227.0 ± 3.0	21.5 ± 0.5	[74]
	BM (T2 copper)	270.0 ± 3.0	25.5 ± 0.3	[74]
NVEBW	without preheating	190.0	-	[72]
	BM (Cu-ETP)	252.4	-	[72]
FSW	without preheating	220.7 ± 0.5	up to 35.0	[75]
	BM (Cu-ETP)	261.2 ± 0.4	up to 30.0	[75]
FSW	without preheating	228.8	24.7	[76]
FSW	without preheating	235.9	15.1	[76]
	BM (“pure copper”)	236.7	27.7	[76]
FSW	without preheating	221.0	-	[77]
	BM (“pure copper”)	254.0	-	[77]
CCGTAW	without preheating	188.0	24.0	[78]
PCGTAW	without preheating	191.0	30.0	[78]
FSW	without preheating	210.0	42.0	[78]
	BM (Cu-ETP)	233.0	49.0	[78]

between the different welding processes are possible. It has to be noted that consistently high mechanical properties were reported for friction stir welding. However, there was no data reported concerning the specific electrical conductivity of the joints. The welding processes that utilized a high power density beam (LBW and EBW) without filler (which was shown to be crucial for maintaining a high specific electrical conductivity) without preheating, show a tendency to low fracture strains, due to the mentioned defects. The applied preheating significantly increased the fracture strain and produced a comparable tensile strength.

The mechanical properties may be further increased by optimizing the preheating process (lower temperatures, smaller affected area). This can be done by using a multi-spot technology, which would utilize a very narrow preheating zone into large penetration depths. Also, the welding process can be stabilized by the application of an appropriate beam oscillation [21, 46] or modulation [14, 47, 48] which would reduce defects.

4 Conclusions

Bead on plate EBW was carried for Cu-ETP. Two welding speed regimes were identified for full penetration welds. A critical welding speed of $v_c \approx$ 320–350 $\mathrm{mm\,s^{-1}}$ was determined which separated the regimes. For lower speeds the required energy input per weld length was mainly influenced by the radial heat conduction. The root formation was disrupted by melt ejections, which were related to the physical phenomena causing spiking. These defects were eliminated by reducing the radial power loss due to preheating and an

increase in welding speed, which elongated the weld pool and reduced the required beam power. Therefore, the overheating of the weld pool was reduced, which, in turn, increased the viscosity and surface tension of the weld pool. This effect led to proper root formation. Also porosity due to spiking was greatly reduced for partial penetration welds. By increasing the welding speed from $v = 40\,\mathrm{mm\,s^{-1}}$ to $v = 200\,\mathrm{mm\,s^{-1}}$ while preheating the weld area, spiking defects were completely avoided in partial penetration welds. Above v_c, the required energy input per weld length was not determined by the radial heat conduction. The melt pool at the top and the bottom of the plate became elongated. This elongation resulted in the formation of a root. However, root humps and melt ejections at the upper bead were observed.

Electrical conductivity was slightly reduced compared to the base metal for welds made below v_c without preheating. The conductivity was lower for welds made above v_c due to the melt ejections at the top. However, conductivity was increased by a subsequent smoothing. For preheated specimens, the changes in microstructure yielded a specific electrical conductivity which was higher than the reference value of the base metal.

UTS were lower for welds made below v_c without preheating and with preheating compared to the base metal. However, the fracture strain of the preheated specimens was significantly higher than that in BM and the welds generated without preheating.

Acknowledgements The authors gratefully acknowledge M. Michler for the support during the ultrasonic testing, P. Hollmann and A. Holst for the realization of the EBSD investigations and A. Möckel for the realization of the resistance measurements.

Funding Open Access funding enabled and organized by Projekt DEAL.

Declarations

Conflict of interest The authors declare no competing interests.

References

1. Kerr RA (2014) The coming copper peak. Science 343(6172):722–724. https://doi.org/10.1126/science.343.6172.722
2. Vidal O, Le Boulzec H, Andrieu B, Verzier F (2022) Modelling the demand and access of mineral resources in a changing world. Sustainability 14(1):11–26. https://doi.org/10.3390/su14010011
3. Martienssen W (2005) In springer handbook of condensed matter and materials data, Martienssen W, Warlimont (eds) H (Springer Berlin Heidelberg, 2005), pp 45–158. https://doi.org/10.1007/3-540-30437-1_4
4. Zhang LJ, Ning J, Zhang XJ, Zhang GF, Zhang JX (2015) Single pass hybrid laser-MIG welding of 4-mm thick copper without preheating. Materials & Design 74:1–18. https://doi.org/10.1016/j.matdes.2015.02.027
5. Zhang G, Zhang L, Kang C, Zhang J (2016) Development of friction stir spot brazing (FSSB). Materials & Design 94:502–514. https://doi.org/10.1016/j.matdes.2016.01.057
6. Zhang LJ, Bai QL, Ning J, Wang JN, Yang XQ, Zhang Yin JX (2016) A comparative study on the microstructure and properties of copper joint between MIG welding and laser-MIG hybrid welding. Materials & Design 110:35–50. https://doi.org/10.1016/j.matdes.2016.07.117
7. Dahlgren A (1997) Study of international published experiences in joining copper and copper-alloys. SKI Report 28(16). https://inis.iaea.org/collection/NCLCollectionStore/_Public/28/050/28050046.pdf
8. Nakamura H, Kawahito Y, Nishimoto K, Katayama S (2015) Elucidation of melt flows and spatter formation mechanisms during high power laser welding of pure titanium. J Laser Appl 27(3):032,012. https://doi.org/10.2351/1.4922383
9. Sanderson A (2007) Four Decades of Electron Beam Development at TWI. Welding in the World 51(1–2):37–49. https://doi.org/10.1007/BF03266547
10. Halbauer L (2020) Beitrag zum Elektronenstrahlfügen von TRIP-Matrix Kompositen: Dissertation, TU Freiberg . https://nbn-resolving.org/urn:nbn:de:bsz:105-qucosa2-708908
11. Yan W, Smith J, Ge W, Lin F, Liu WK (2015) Multiscale modeling of electron beam and substrate interaction: a new heat source model. Comput Mech 56(2):265–276. https://doi.org/10.1007/s00466-015-1170-1
12. Zenker R (1996) Electron beam surface treatment: industrial application and prospects. Surf Eng 12(4):296–297. https://doi.org/10.1179/sur.1996.12.4.296
13. Tsukamoto S, Kawaguchi I, Arakane G, Honda H (2001) In: International congress on applications of lasers & electro-optics (Laser Institute of America, Orlando, Florida, 2001), pp 400–408. https://doi.org/10.2351/1.5059890
14. Heider A, Weber R, Graf T (2012) In: International congress on applications of lasers & electro-optics (Laser Institute of America, 2012), pp 532–538. https://doi.org/10.2351/1.5062504
15. Arata Y, Kiyoshi T, Shozo M (1974) Study on characteristics of weld defect and its prevention in electron beam welding (Report III) : characteristics of cold shut. Transactions of JWRI 3(2):207–214 . http://hdl.handle.net/11094/10251
16. O'Brien TP, Pence PE, Funk ER, McMaster RC (1974) Suppression of spiking in partial penetration EB welding with feedback control. Welding Journal (suppl.) 53:32–338 . https://app.aws.org/wj/supplement/WJ_1974_08_s332.pdf
17. Abdul Jawwad AK, Strangwood M, Davis CL (2005) Microstructural modification in full penetration and partial penetration electron beam welds in INCONEL-718 (IN-718) and its effect on fatigue crack initiation. Metallurgical and Materials Trans A 36(5):1237–1247. https://doi.org/10.1007/s11661-005-0216-y

18. Liang L, Hu R, Wang J, Luo M, Huang A, Wu B, Pang S (2019) A CFD-FEM model of residual stress for electron beam welding including the weld imperfection effect. Metall and Mater Trans A 50(5):2246–2258. https://doi.org/10.1007/s11661-019-05154-8
19. Arata Y, Matsuda F, Murakami T (1973) Some dynamic aspects of weld molten metal in electron beam welding. Transactions of JWRI 2(2):152–161. http://hdl.handle.net/11094/12064
20. Pastor M, Zhao H, DebRoy T (2001) Pore formation during continuous wave Nd:YAG laser welding of aluminium for automotive applications. Weld Int 15(4):275–281. https://doi.org/10.1080/09507110109549355
21. Kanigalpula P, Jaypuria S, Pratihar DK, Jha MN (2018) Experimental investigations, input-output modeling, and optimization of spiking phenomenon in electron beam welding of ETP copper plates. Measurement 129:302–318. https://doi.org/10.1016/j.measurement.2018.07.040
22. Jaypuria S, Gupta SK, Pratihar DK, Chakrabarti D, Jha MN (2020) In: Advances in materials and manufacturing engineering, by Li L, Pratihar DK, Chakrabarty S, Mishra PC, (eds) Lecture Notes in Mechanical Engineering (Springer Singapore, Singapore, 2020), pp 405–411. https://doi.org/10.1007/978-981-15-1307-7_45
23. Enzinger N, Loidolt P, Wiednig C, Stütz M, Sommitsch C (2017) Electron beam welding of thick-walled copper components. Sci Technol Weld Joining 22(2):127–132. https://doi.org/10.1080/13621718.2016.1204516
24. Stummer M, Stütz M, Aumayr A, Enzinger N (2018) Electron beam welding of copper using plasma spraying for filler metal deposition. Welding in the World 62(6):1341–1350. https://doi.org/10.1007/s40194-018-0637-z
25. Armstrong RE (1970) Control of spiking in partial penetration electron beam welds. Welding Journal (suppl.) 49:382–388 . http://files.aws.org/wj/supplement/WJ_1970_08_s382.pdf
26. Sandstorm DJ, Buchen JF, Hanks GS (1970) On the measurement and interpretation and application of parameters important to electron beam welding. Welding Journal (suppl.) 49:293–300 . https://app.aws.org/wj/supplement/WJ_1970_07_s293.pdf
27. Phadke MS, Joglekar AM, Wu SM (1977) Investigation of spiking in electron beam welding using stationary stochastic models. J Eng Industry 99(2):323–326. https://doi.org/10.1115/1.3439216
28. Tong H, Giedt WH (1970) A dynamic interpretation of electron beam welding. Welding Journal (suppl.) 49:159–166 . https://app.aws.org/wj/supplement/WJ_1970_06_s259.pdf
29. Tsukamoto S, Irie H (1993) Melting process and spiking phenomenon in electron beam welding. Transcations of the Japan Welding Society 24(1):18–23 . https://dl.ndl.go.jp/view/download/digidepo_10945846_po_ART0003859815.pdf?contentNo=1&alternativeNo=
30. Arata Y, Fujisawa M, Abe E (1976) A study on dynamic behaviours of electron beam welding (Report I): The observation by a fluoroscopic method. Transactions of JWRI 5(1):1–9 . http://hdl.handle.net/11094/10360
31. Wei PS, Chuang KC, Ku JS, DebRoy T (2012) Mechanisms of spiking and humping in keyhole welding. IEEE Trans Components, Packaging Manufact Technol 2(3):383–394. https://doi.org/10.1109/TCPMT.2011.2178412
32. Tong H, Giedt WH (1971) Depth of penetration during electron beam welding. J Heat Transfer 93(2):155–163. https://doi.org/10.1115/1.3449777
33. Weber CM, Funk ER, McMaster RC (1972) Penetration mechanism of partial penetration electron beam welding. Weld Journal (suppl.) 51:90–94. https://app.aws.org/wj/supplement/WJ_1972_02_s90.pdf
34. Mara GL, Funk ER, McMaster RC, Pence PE (1974) Penetration mechanisms of electron beam welding and the spiking phenomenon. Weld Journal (suppl.) 53:246–251 . http://files.aws.org/wj/supplement/wj_1974_06_s246.pdf
35. Arata Y, Tomie M, Abe N, Yao XY (1987) Observation of Molten Metal Flow during EB Welding(Physics, Process & Instrument). Transactions of JWRI 16(1):13–16 . http://hdl.handle.net/11094/12081
36. Schauer DA, Giedt WH (1978) Prediction of electron beam welding spiking tendency. Welding Journal (suppl.) 57:189–195 . https://app.aws.org/wj/supplement/WJ_1978_07_s189.pdf
37. Zhang LJ, Zhang JX, Gumenyuk A, Rethmeier M, Na SJ (2014) Numerical simulation of full penetration laser welding of thick steel plate with high power high brightness laser. J Mater Process Technol 214(8):1710–1720. https://doi.org/10.1016/j.jmatprotec.2014.03.016
38. Pang S, Chen L, Zhou J, Yin Y, Chen T (2011) A three-dimensional sharp interface model for self-consistent keyhole and weld pool dynamics in deep penetration laser welding. J Phys D: Applied Phys 44(2):025,301. https://doi.org/10.1088/0022-3727/44/2/025301
39. Otto A, Vázquez RG, Hartel U, Mosbah S (2018) Numerical analysis of process dynamics in laser welding of Al and Cu. Procedia CIRP 74:691–695. https://doi.org/10.1016/j.procir.2018.08.040
40. Liu C, He J (2016) Numerical analysis of fluid transport phenomena and spiking defect formation during vacuum electron beam welding of 2219 aluminium alloy plate. Vacuum 132:70–81. https://doi.org/10.1016/j.vacuum.2016.07.033
41. Chen G, Liu J, Shu X, Gu H, Zhang B (2019) Numerical simulation of keyhole morphology and molten pool flow behavior in aluminum alloy electron-beam welding. Int J Heat Mass Transf 138:879–888. https://doi.org/10.1016/j.ijheatmasstransfer.2019.04.112
42. Yang Z, Fang Y, He J (2020) Numerical investigation on molten pool dynamics and defect formation in electron beam welding of aluminum alloy. J Mater Eng Perform 29(10):6570–6580. https://doi.org/10.1007/s11665-020-05111-2
43. Fetzer F, Hu H, Berger P, Weber R, Eberhard P, Graf T (2018) Fundamental investigations on the spiking mechanism by means of laser beam welding of ice. J Laser Appl 30(1):1–9. https://doi.org/10.2351/1.4986641
44. Wei PS, Chuang KC, DebRoyT KuJS (2011) Scaling of spiking and humping in keyhole welding. J Phys D: Applied Phys 44(24):245,501. https://doi.org/10.1088/0022-3727/44/24/245501
45. Trushnikov DN, Koleva EG, Mladenov GM, Belenkiy VY (2013) Effect of beam deflection oscillations on the weld geometry. J Mater Process Technol 213(9):1623–1634. https://doi.org/10.1016/j.jmatprotec.2013.03.028
46. Luo M, Hu R, Liu T, Wu B, Pang S (2018) Optimization possibility of beam scanning for electron beam welding: Physics understanding and parameters selection criteria. Int J Heat Mass Transf 127:1313–1326. https://doi.org/10.1016/j.ijheatmasstransfer.2018.07.014
47. Heider A, Hess A, Weber R, Graf T (2011) In International congress on applications of lasers & electro-optics (Laser Institute of America, 2011), pp 395–402. https://doi.org/10.2351/1.5062263
48. Heider A, Weber R, Herrmann D, Herzog P, Graf T (2015) Power modulation to stabilize laser welding of copper. J Laser Appl 27(2):1–8. https://doi.org/10.2351/1.4906127
49. Cho JH, Farson DF, Reiter MJ (2009) Analysis of penetration depth fluctuations in single-mode fibre laser welds. J Phys D Appl Phys 42(11):1–8. https://doi.org/10.1088/0022-3727/42/11/115501
50. Arata Y (1983) In: 1st European conf on cineradiography with photons or particles, by Marilleau JJ (ed) (SPIE, 1983), SPIE Proceedings, pp 50–57. https://doi.org/10.1117/12.932912
51. Halbauer L, Proksch P, Buchwalder A, Zenker R, Biermann H (2018) Joining of TWIP-matrix composites by electron beam brazing. Welding in the World 62(1):19–27. https://doi.org/10.1007/s40194-017-0519-9
52. Brueggemann G, Benziger T (1996) In: Laser processing of materials and industrial applications, by Deng SS, Wang SC (ed)

(SPIE, 1996), SPIE Proceedings, p 168. https://doi.org/10.1117/12.253099
53. Chattopadhyay A, Muvvala G, Sarkar S, Racherla V, Nath AK (2022) Microstructure, mechanical, and corrosion properties of electron beam-welded commercially pure titanium after laser shock peening. The Intern J Adv Manufact Technol 118(1–2):343–364. https://doi.org/10.1007/s00170-021-07955-x
54. Otten C, Reisgen U, Schmachtenberg M (2016) Electron beam welding of aluminum to copper: mechanical properties and their relation to microstructure. Welding in the World 60(1):21–31. https://doi.org/10.1007/s40194-015-0280-x
55. Li L, Wang S, Huang W, Jin Y (2020) Microstructure and mechanical properties of electron beam welded TC4/TA7 dissimilar titanium alloy joint. J Manuf Process 50:295–304. https://doi.org/10.1016/j.jmapro.2019.11.007
56. Halbauer L, Laubstein R, Radajewski M, Buchwalder A, Krüger L, Biermann H (2019) Electron beam welding and characterization of dissimilar joints with TWIP matrix composites. Advanced Engineering Materials 21(5):1800,586. https://doi.org/10.1002/adem.201800586
57. Swift-Hook DT, Gick AEF (1973) Penetration welding with lasers. Weld Journal (suppl.) 52: 492–499 . http://files.aws.org/wj/supplement/WJ_1973_11_s492.pdf
58. Ganser A, Pieper J, Liebl S, Zaeh MF (2016) Numerical simulation of the thermal efficiency during laser deep penetration welding. Phys Procedia 83:1377–1386. https://doi.org/10.1016/j.phpro.2016.08.144
59. Borrmann S, Kratzsch C, Halbauer L, Buchwalder A, Biermann H, Saenko I, Chattopadhyay K, Schwarze R (2019) Electron beam welding of CrMnNi-steels: CFD-modeling with temperature sensitive thermophysical properties. Int J Heat Mass Transf 139:442–455. https://doi.org/10.1016/j.ijheatmasstransfer.2019.04.125
60. Rai R, Burgardt P, Milewski JO, Lienert TJ, DebRoy T (2009) Heat transfer and fluid flow during electron beam welding of 21Cr-6Ni-9Mn steel and Ti-6Al-4V alloy. J Phys D: Applied Phys 42(2):025,503. https://doi.org/10.1088/0022-3727/42/2/025503
61. Rai RR, Plamer TA, Elmer JW, DebRoy T (2009) Heat transfer and fluid flow during electron beam welding of 304L stainless steel alloy. Welding Journal 88:54–61 . https://app.aws.org/wj/supplement/WJ_2009_03_s54.pdf
62. Cardarelli F (ed.) (2008) Materials handbook: A concise desktop reference, 2nd edn. (Springer, London, 2008). https://doi.org/10.1007/978-1-84628-669-8
63. Kazemi K, Goldak JA (2009) Numerical simulation of laser full penetration welding. Comput Mater Sci 44(3):841–849. https://doi.org/10.1016/j.commatsci.2008.01.002
64. Seto N, Katayama S, Matsunawa A (2002) Porosity formation mechanism and reduction method in CO 2 laser welding of stainless steel. Weld Int 16(6):451–460. https://doi.org/10.1080/09507110209549558
65. Zhang R, Tang X, Xu L, Lu F (2020) Cui H, Study of molten pool dynamics and porosity formation mechanism in full penetration fiber laser welding of Al-alloy. Intern J Heat Mass Transfer 148:119,089. https://doi.org/10.1016/j.ijheatmasstransfer.2019.119089
66. Heider A (2018) Erweitern der Prozessgrenzen beim Laserstrahlschweißen von Kupfer mit Einschweißtiefen zwischen 1 mm und 10 mm: Zugl.: Dissertation, Stuttgart, Univ. , 2018. Laser in der Materialbearbeitung (utzverlag, München, 2018). https://www.utzverlag.de/assets/pdf/44738dbl.pdf
67. Fabbro R (2010) Melt pool and keyhole behaviour analysis for deep penetration laser welding. J Phys D: Applied Phys 43(44):445,501. https://doi.org/10.1088/0022-3727/43/44/445501
68. Berger P, Hügel H, Hess A, Weber R, Graf T (2011) Understanding of humping based on conservation of volume flow. Phys Procedia 12:232–240. https://doi.org/10.1016/j.phpro.2011.03.030
69. Schulze G (ed.) (2010) Die Metallurgie des Schweißens (Springer Berlin Heidelberg, Berlin, Heidelberg, 2010). https://doi.org/10.1007/978-3-642-03183-0
70. Ning J, Zhang LJ, Wang QL, Bai JN, Yang JX, Zhang, (2016) Effects of double-pass welding and extrusion on properties of fiber laser welded 1.5-mm thick T2 copper joints. J Materials Process Technol 237:75–87. https://doi.org/10.1016/j.jmatprotec.2016.06.011
71. Zhang LJ, Zhang GF, Ning J, Zhang XJ, Zhang JX (2015) Microstructure and properties of the laser butt welded 1.5-mm thick T2 copper joint achieved at high welding speed. Materials & Design 88:720–736. https://doi.org/10.1016/j.matdes.2015.09.072
72. Hassel T, Beniyash A, Klimov G (2020) Non-vacuum electron beam welding and cutting of cupper. IOP Conference Series: Materials Science and Engineering 759(1):012,003. https://doi.org/10.1088/1757-899X/759/1/012003
73. Din EN (2014-12) 13599:2014-12. Copper and Copper alloys - Copper plate, sheet and strip for electrical purposes. https://doi.org/10.31030/2251682
74. Chen Y, Chen C, Gao M, Zeng X (2016) Achieving high strength joint of pure copper via laser-cold metal transfer Arc hybrid welding. Metall and Mater Trans A 47(6):2866–2874. https://doi.org/10.1007/s11661-016-3497-4
75. Machniewicz T, Nosal P, Korbel A, Hebda M (2020) Effect of FSW traverse speed on mechanical properties of copper plate joints. Materials (Basel, Switzerland) 13(8). https://doi.org/10.3390/ma13081937
76. Xue P, Xie GM, Xiao BL, Ma ZY, Geng L (2010) Effect of Heat Input Conditions on Microstructure and Mechanical Properties of Friction-Stir-Welded Pure Copper. Metall and Mater Trans A 41(8):2010–2021. https://doi.org/10.1007/s11661-010-0254-y
77. Lee WB, Jung SB (2004) The joint properties of copper by friction stir welding. Mater Lett 58(6):1041–1046. https://doi.org/10.1016/j.matlet.2003.08.014
78. Amarnath V, Karuppuswamy P, Balasubramanian V (2017) Comparative study of joining processes of high conductivity electrolytic tough pitch copper used in automotive industries. Intern J Vehicle Structures Syst 9(1). https://doi.org/10.4273/ijvss.9.1.01